

**Planetary Defense Conference 2013
Flagstaff, USA**

**IAA-PDC13-05-05
Low-Altitude Atmospheric and Water-Surface Effects of Small Impacts**

Galen Gisler⁽¹⁾

⁽¹⁾*Physics of Geological Processes, University of Oslo, PO Box 1048 Blindern, 0316 Oslo, Norway
+47 9989 8013 or +1 505 920 2722, galen.gisler@fys.uio.no*

Keywords: *atmospheric effects of impacts, airbursts, impact tsunamis, hydrocodes*

ABSTRACT

The atmospheric effects associated with the impact of a 125 m asteroid are considerably worse than the effects associated with the wave such an impact into water can produce, unless the impact occurs within a few tens of kilometers of a shoreline (Gisler et al. 2011, Gisler 2011). In the present study, we calculate the energy deposition into atmosphere and water from the impacts of asteroids with diameters 125 m, 40 m, and 5 m in both airburst and non-airburst scenarios. The airburst impacts are calculated by assuming that 10% of the asteroid's initial kinetic energy is converted into an explosive airburst at an altitude of 10 km. In the 125 m and 40 m non-airburst impacts, a substantial water splash is produced, yielding a strongly nonlinear wave that decays strongly. In the corresponding airburst events, the pressure pulse is distributed over a broader water surface, resulting in more gentle and coherent wave-like motion that may lead to a propagating wave. In both airburst and non-airburst cases, a very large quantity of water vapor is produced and lofted into the stratosphere, which may lead to long-lasting climate effects. For the smallest event, the 5-m asteroid, there is very little difference between the airburst and non-airburst case. Our two smaller airburst events are comparable to the actual airburst from the Chelyabinsk meteor of 15 February 2013, and our results offer relevant insights.

1. Introduction

We present calculations with the Sage hydrocode (Gittings *et al.* 2008) of asteroid impacts over water in airburst and non-airburst scenarios, for comparison purposes. Sage was developed by Michael Gittings at Science Applications International and further adapted and developed at Los Alamos National Laboratory. We have previously applied this code to tsunami generation from landslides (Gisler et al 2006a), from submarine volcanos (Gisler et al 2006b), and from asteroid impacts (Gisler 2009, Gisler et al 2003). More recently, it has also been applied to the physics of supercritical fluid eruptions (Gisler 2011) and to the eruptions of volatile-rich magmatic columns (Gisler, Galland, and Haug 2013 in preparation). Sage runs in 2- or 3-dimensions, can use either analytical or tabular equations of state, and contains a simple strength model (which is not used in these calculations).

This study considers the lower-atmospheric and water-surface effects of an impact into a deep ocean or an airburst above the ocean, so the problem domain naturally consists of (1) the atmosphere, up to some height above which there is negligible influence on lower-atmospheric and water-surface effects; (2) the water, down to its bottom; and (3) the impacting asteroid itself. We make the domain large enough so that acoustic and pressure waves reflected from the boundaries have little influence on the effects we desire to observe, so the domain size therefore depends on the magnitude of the impact event.

All components of the problem (atmosphere, water, and asteroid) are assumed to be strengthless. For the atmosphere and the water, this assumption is clearly valid. For the asteroid, it is not so obvious. However, the dynamical pressure of reentry at the typical speeds of impact (20 km/s or greater) greatly exceed the material strength corresponding to the composition and structure of most asteroids so that the strengthless assumption is not too bad. The asteroid is also assumed to be initially spherical, a much more questionable assumption. The atmosphere and the water are assumed to be initially at rest, homogeneous, and in hydrostatic equilibrium, using a standard temperature profile for the atmosphere.

In the present calculations, the asteroid is initialised at an altitude of 10 km, with a vertical downward velocity of 20 km/s. We assume a vertical trajectory so that we can run Sage in two dimensions under the assumption of cylindrical symmetry.

In the airburst runs, the asteroid is assumed to dissipate 10% of its kinetic energy at the initial 10 km altitude in a single explosion that results in the asteroid blowing itself apart, with the fragments continue downwards conserving momentum. We don't calculate the details of the disruption, but simply assume that the dynamic pressure reached when the asteroid encounters the denser atmosphere is greater than the asteroid's residual

cohesive strength, and an explosion occurs. We do not consider whether the conversion of kinetic energy to explosive energy is greater or less than 10%. In the 15 February 2013 Chelyabinsk event a succession of 3 such explosions at 15-25 km altitude apparently consumed a much larger fraction of its initial kinetic energy (Yeomans and Chodas 2013). The flatness of the Chelyabinsk meteor's trajectory may have contributed to the multiple explosions.

2. The computational technique

The central assumptions of the Sage hydrocode are that nature may be treated as a continuum, that mass, momentum, and energy are conserved, and that mixing and other microscopic processes occur quickly enough that local thermodynamic equilibrium is preserved on small spatial scales. The version of Sage that we use is concerned solely with dynamics, kinetics, and thermodynamics. Chemical processes, radiation, and electromagnetics are ignored, although these could be included in further studies. The only mechanisms of heat transport are advection and convection.

Sage is an Eulerian code, and divides the computational domain into a large number of fixed, square, regular computational cells. The principal physical quantities associated with each cell are the density, pressure, momentum, and internal energy per unit mass of the material within the cell. In addition there are material identifiers associated with the cell, indicating how much each material in the problem contributes to the pressure and density within the cell. All these quantities are advanced from one time step to the next using the Euler equations:

$$\begin{aligned}\frac{\partial \rho}{\partial t} + \nabla \cdot (\rho \vec{u}) &= 0 \\ \frac{\partial \rho \vec{u}}{\partial t} + \nabla \cdot (\rho \vec{u} \vec{u}) + \nabla \cdot \vec{\sigma} &= \rho \vec{g} \\ \frac{\partial \rho E}{\partial t} + \nabla \cdot (\rho \vec{u} E) + \nabla \cdot (\vec{\sigma} \vec{u}) &= 0 \\ \vec{\sigma} &= F(\rho, E, \text{history}, \dots)\end{aligned}$$

The first of these is the continuity equation (conservation of mass), relating the change with time of local density ρ to the divergence of momentum (vector u is velocity). Next is the equation of motion (conservation of momentum), relating the local rate of change of momentum to the divergence of momentum flux, the divergence of the stress tensor σ (which reduces to pressure, for strengthless materials), and the acceleration due to gravity g . Third is the equation of conservation of energy (E is total energy per unit mass), depending on the fluxes of energy and stress.

The final, schematic, equation is necessary to close the Euler set. It relates the stress (or pressure) supported by a material to the intensive properties density, total specific energy, and material history. As used here for strengthless materials, history is not relevant, and this schematic equation simplifies to yield pressure as a function of density and temperature, just an equation of state.

Equations of state in the Sage code can be analytical or tabular, and come from a variety of sources. The three materials in the present problem (air, water, and asteroid) are all treated using tabular equations of state. For air and asteroid (assumed to be basaltic composition) we use the tabular SESAME equations of state from Los Alamos National Laboratory (Lyon and Johnson 1992). For water, we use an equation of state that is contained within the Sage code itself, derived by SAIC from the NBS/NIST steam tables (Haar, Gallagher, and Kell 1984). The equations of state for basalt and water are illustrated in Figure 1.

At the beginning of each simulation, regions are set up within the problem domain that contain air, water, and asteroid, with no mixed cells. As the simulations progress, asteroid material mixes first with the air, and eventually with the water, and air and water mix at their interface. Each cell in the problem then potentially has up to three different materials within it. Mixing within a cell is assumed to result in local thermodynamic equilibrium, with each material contributing its partial volume and partial pressure to the cell. In this way a single temperature and velocity is arrived at for each cell. Thus Sage is a *multi-material*, but not a *multi-phase* or *multi-fluid* code.

Sage uses the technique of continuous adaptive mesh refinement (CAMR). If the gradient across a cell, in any of the physical quantities, exceeds a particular threshold, the cell is subdivided into 4 equal smaller cells (in two dimensions; in three dimensions it would be subdivided into 8 subcells). This refinement occurs on every timestep. Conversely, when gradients across a group of subcells are reduced below a similar but lower threshold, those subcells are recombined into their parent cells. The CAMR technique enables calculations to be done with exquisite precision in regions which require it, at minimum computational cost.

The conservation laws expressed by the Euler equations above are solved using a finite-volume scheme. Cell-centred quantities for mass, momentum, and energy are considered as average quantities over the cell volume, with changes exactly balanced by fluxes across cell boundaries. At each cell boundary, a Riemann problem propagates discontinuities in mass, momentum, and energy as waves into future space-time. Combining the waves from neighbouring cell boundaries yields future values of the cell-based quantities. For details on how finite-volume methods work, see Leveque (2002). This procedure is carried out at every cell at every timestep. Conservation of mass, momentum, and energy is maintained at machine accuracy, and monitored.

3. Results of the Present Study

In the present study, we have run Sage simulations of the cases illustrated in the following table. These calculations were run on a computer cluster, Stallo, at the University of Tromsø in northern Norway, with computer time provided by the Norwegian Metacentre for High-Performance Computing, Notur. Running on 64 processors of the Stallo cluster, some runs took up to a month of continuous computation to calculate the problem out to 100 seconds of physical time. The calculations are two-dimensional, with cylindrical symmetry about the vertical impact trajectory. They naturally miss features that are inherently three-dimensional, including effects of a non-vertical trajectory and Coriolis forces. All calculations were performed with the continuous adaptive mesh refinement ability of the Sage code, with a largest refinement factor of 8 powers of 2 or 256, so very fine structures in the atmosphere and water surface are resolved. The largest of these calculations was performed in a problem domain measuring 32 km in the horizontal (radial) direction and 44 km in the vertical direction, and a smallest grid spacing of 3.125 m; the smallest calculations (for the 5-m impactors) were run in a domain 4 km in radius by 12 km in height, and a smallest grid spacing of 31.25 cm. In all cases, the asteroid was started intact at an altitude of 10 km and with a downward velocity of 20 km/s. For the airburst cases, the explosion was initiated at the beginning of the calculation.

run	diameter (m)	height of burst (km)	speed (km/s)	explosion energy (kt)	kinetic energy (kt)	total energy (kt)	max pressure at 2 km (bar)	max pressure at 4 km (bar)
iAb5	125	10	-20	9 777	97 768	107 545	42.5	8.8
iAc5	40	10	-20	320	3 204	3 524	1.7	1.5
iAd5	5	10	-20	0.63	6.26	6.88	1.02	1.03
iAw5	125	no burst	-20	0	107 545	107 545	42.5	4.7
iAv5	40	no burst	-20	0	3 524	3 524	8.9	1.9
iAu5	5	no burst	-20	0	6.88	6.88	1.02	1.02

The six runs are in pairs, one with an airburst converting 10% of the initial kinetic energy into explosive energy at 10 km altitude, and the other without such an airburst, so that it proceeds downward suffering only ablative losses. In all runs, the impact event is considered to occur over an ocean of 5 km depth.

The paired runs (iAb5-iAw5, iAc5-iAv5, iAd5-iAu5) were designed with diameters of 125m, 40m, and 5m respectively, and the same total energy in each pair. The first member of each pair was performed with an airburst, the second without. The total energy is conceived to be the pre-atmospheric kinetic energy of the asteroid.

We first examine the energy deposition into the atmosphere and the water for the six runs. These histories are shown, in logarithmic scale, in Figure 2. We plot the kinetic energies only, because the effect shows up most immediately in this mode, and conversion to other forms of energy (potential, internal, and radiative) follows rapidly. As expected, the large events deposit considerably more energy into atmosphere and water than the smaller events, and the airburst events deliver energy to the atmosphere much more efficiently and quickly than the non-airburst events, except for the smallest, 5-m impact, where there is very little difference between the two cases. Ablation of the asteroid during the atmospheric passage of the two smaller non-airburst impacts is significant.

Energy delivery to the water surface is significantly greater, and faster, in the non-airburst cases, except (once again) for the smallest case, in which there is essentially no difference. In the 5-m impact non-airburst case, the effect of atmospheric ablation of the projectile is nearly the same as the effect of an explosion, with the difference that the impulse due to ablation is spread out over a few seconds' duration.

In Figure 3 we illustrate the ground-level pressure profiles with time for each of these six runs, from tracer particles distributed over the water surface and 50 m below. For the largest (125 m) events, a ground level pressure of the order of 100 atmospheres is recorded in the airburst event and less than half that in the non-airburst event. In the airburst case, a greater number of tracer particles participate in the very high pressures because the impulse is spread over a larger area. There is a similar effect for the intermediate (40 m) event, except that the greatest impulsive pressure experienced in the non-airburst impact is nearly twice as large as in the airburst case. These impulsive high pressures are mostly in the immediate vicinity of the impact point. In the smallest (5 m) pair, the airburst case sees larger and highly fluctuating pressures for a full minute following the explosion. The pressures experienced in this event go up to 3500 Pascals, or 3.5% atmospheric pressure, and may be capable of breaking glass in windows at ground level. The Chelyabinsk event of 15 February 2013, in which the breaking of glass led to many injuries, provides an opportunity for validating simulations.

Lower-atmospheric and water-surface effects are illustrated by graphics of temperature and density in a region surrounding the impact point, and by the trajectories of the racer particles. In Figures 4 through 13 we show these for the six runs of our study.

The airburst for the largest impact event we ran (125 m projectile) was an explosion of 9 777 kilotons magnitude at an altitude of 10 km (Figure 4). This resulted in ground-level pressure of 10-100 atmospheres, spread over 5 kilometres from the projected impact point. The projectile's momentum carried the impulse to ground-level, and produced a weak transient crater of less than 100-m depth. By the time of Figure 4, the transient crater has rebounded to a small mound, and temperatures near the impact point have cooled to 3000 K from an initial high of 6500 K. Considerable evaporation of surface water has occurred behind the hot blast front which by the time of Figure 4 has expanded out to 30 km radius. A strong centre-focussed wind inhibits the growth and propagation of a surface wave. In 3-dimensions this wind leads to a strong anti-cyclone carrying much of the evaporated water skyward.

Tracer particle trajectories in this calculation (Figure 5) illustrate potential wave-like behaviour beneath the surface, where the momentum transmitted to the water is less influenced by surface evaporation and atmospheric effects. At 4 km distance from the impact point, the amplitude of this subsurface wave is approximately 10 m, and it is likely to propagate.

A 125-m asteroid that impacts the water directly produces a much more substantial effect on the water surface (Figure 6). A transient crater forms, reaching a maximum depth of about 1.2 km at 5 seconds after calculation start. Temperatures generated during impact can be as high as in the airburst case, but the heat is much more closely confined to the impact site, and produces a hot plume that ascends out the impact channel into the stratosphere. The crown splash reaches high into the atmosphere and injects water vapour and dissociated asteroid material into the stratosphere. Following the collapse of the crown splash, a rebound jet forms and collapses to become a substantial nonlinear wave by the time shown in Figure 5. Evaporation of water within the transient crater produces a hot and turbulent atmosphere that strongly modifies the wave and inhibits its growth and propagation.

The strong nonlinearity of the wave is demonstrated in the tracer-particle trajectory plot (Figure 7), which shows some coherency in the under-surface tracers, but nearly chaotic motion in the tracers on the surface. From this calculation it is difficult to assess the likelihood of long-distance propagation of the wave that is produced from the impact, but such non-coherent and non-linear waves are very different from classical tsunamis that arise from underwater earthquakes and landslides. These giant splash waves are similar to those produced in fjord-wall collapse scenarios, very devastating in the near field, but insignificant in the far field.

The 40-m asteroid that experiences an airburst at 10 km (Figures 8 and 9) produces no perceptible transient water crater. The atmospheric blast wave reaches the surface and rebounds, with the hottest part of the plume merely touching the water surface, reaching a temperature above 100 K. The pressure pulse produces a slight disturbance, and a wave of about 1 m amplitude forms, as shown by the tracers. The hot plume eventually dissipates into the upper atmosphere.

The impact of a 40-m asteroid that is not destroyed by an airburst results in a small transient crater, approximately 400 m deep. The hot plume produced during atmospheric passage and impact ascends into the upper atmosphere, leaving a strong atmospheric disturbance that interacts with the water surface (Figures 10 and 11). The collapse of the rebound jet produces a modest breaking wave that propagates away from the impact point, though it decays rapidly as it recedes. At a distance of 4 km, this wave has an amplitude of about 40 m, seen best in the lower-level tracers of Figure 11.

The two calculations of 5-m asteroids, with and without airbursts, show few differences (Figures 12 and 13). With an airburst, a blast wave is produced at high altitude and propagates down into the lower atmosphere while the thermal plume dissipates into space. The pressure pulse may be sufficient to break windows at ground level in the immediate vicinity. Without an airburst, the hot plume is more persistent because ablation occurs gradually as the projectile penetrates lower into the atmosphere, but the pressure pulse is weaker and more localised. Stagnation occurs at an altitude of about 5 km. In both cases a small wave of about 30 cm amplitude results, but this is of short wavelength and will merge with ordinary storm and wind-produced waves and will not be distinguishable at great distance.

4. Conclusions

For projectile sizes of 100 m and greater, airbursts make the impact atmospheric effects more severe and more widespread, out to hundreds of kilometers. Non-airburst impacts produce more intense local effects, but those effects die off within tens of kilometers.

For projectile sizes less than 10 m, projectile ablation in the atmosphere and airbursts produce almost identical results, with plume stagnation occurring a few kilometers above the surface, and particles falling to the ground thereafter. Nevertheless, pressure waves can break windows within a few kilometers of the impact epicentre.

For intermediate projectile sizes, as we have seen with the Chelyabinsk event, an airburst can produce injuries and damage if it occurs over a populated region, but wide-spread damage is not expected.

As we have shown in previous studies (Gisler 2009, 2011), direct water impacts of asteroids up to a few hundred meters in size produce highly nonlinear “megatsunamis” similar to the Lituya Bay event of 1958 (Mader & Gittings 2002), and the Tafjord event of 1934 (Harbitz et al. 1993). These megatsunamis are devastating in the near field, but do not cause widespread damage as they attenuate and disperse rapidly. At distances greater than a few tens of kilometers the wave effects from such impacts will be comparable to surges due to large tropical storms, which can be locally catastrophic. The effects of blast waves, pressure waves, and thermal atmospheric disturbances will be worse than the surface-water effects at large distances.

On the other hand, airbursts are more likely than non-airburst impacts to cause tsunamis because the pressure pulse transmitted by the incoming projectile’s momentum is spread over a larger area than that of the impact crater. The overall amplitude of the initial water surface disturbance is also less, implying that nonlinear dissipative effects will be correspondingly diminished.

Whether an airburst occurs, and how efficient it is at reducing the asteroid’s kinetic energy, depends on characteristics of the atmosphere and the asteroid itself that will most likely be unknown until the time of atmospheric entry. The asteroid’s shape, its orientation and rotation state, its composition and strength will be determining factors, as will local barometric pressure, wind stratification and speeds. Since small impacts are much more common than large ones, and cause a great deal of public interest and concern, more attention needs to be paid to the range of impacts with sizes less than a few tens of meters.

Domains of hydrocodes used for calculating impact effects rarely extend out beyond a few tens of kilometers. For larger impacts, where such effects might well be felt further afield, it is necessary to pass the result of hydrocode calculations to atmospheric models capable of handling impulsive inputs, and (in the case of water impacts) to wave propagation models.

Acknowledgments

Support from the ESA office of Space Situational Awareness and the use of computers at the University of Tromsø through the Norwegian Metacentre for High Performance Computing are gratefully acknowledged. The Centre for the Physics of Geological Processes is a Centre of Excellence established by the Research Council of Norway.

References

Gittings M.L., Weaver R.P., Clover M., Betlach T., Byrne N., et al., 2008. The RAGE radiation-hydrodynamic code, Los Alamos National Laboratory Report LA-UR-06-0027, Los Alamos, New Mexico, published in Computational Science and Discovery 1, 015005.

G Gisler, R Weaver, M Gittings, Sage Calculations of the Tsunami Threat from La Palma, Science of Tsunami Hazards, 24, 288-301 (2006).

G Gisler, R Weaver, M Gittings, Two-Dimensional Simulations of Explosive Eruptions of Kick-Em Jenny and Other Submarine Volcanos, Science of Tsunami Hazards, 25, 34 (2006).

Gisler, G (2009). Simulations of the explosive eruption of superheated fluids through deformable media. Marine and Petroleum Geology Journal, Special Issue Volume 26, pp1888-1895.

Gisler, G., Weaver, R., Gittings, M. 2011, Calculations of asteroid impacts into deep and shallow water, *Pure and Applied Geophysics*, Volume 168, 1187-1198, DOI: 10.1007/s00024-010-0225-7.

Haar, L., Gallagher, J.S., Kell, G. S., 1984, *NBS/NRC Steam Tables: Thermodynamic and Transport Properties and Computer Programs for Vapor and Liquid State of Water in SI Units*, McGraw-Hill, ISBN 0-89116-354-9.

Harbitz, C., Pedersen, G., and Gjevik, B. (1993). "Numerical Simulations of Large Water Waves due to Landslides." *J. Hydraul. Eng.*, Volume 119(12), pp 1325–1342.

Leveque, R.J. 2002, *Finite Volume Methods for Hyperbolic Problems*, Cambridge Texts in Applied Mathematics

Lyon, S.P., Johnson, J.D. 1992, *Sesame: the Los Alamos National Laboratory equation of state database*, Los Alamos National Laboratory Report LA-UR-92-3407, Los Alamos, New Mexico.

Mader, C.L.; Gittings, M.L. Modeling the 1958 Lituya Bay Mega-tsunami, *Science of Tsunami Hazards*, Volume 20, pp 241-246.

Yeomans, Don; Chodas, Paul (1 March 2013). "[Additional Details on the Large Fireball Event over Russia on Feb. 15, 2013](#)". NASA/JPL Near-Earth Object Program Office.

Copyright © 2013 International Academy of Astronautics.

(No copyright is asserted in the United States under Title 17, US Code. The US Government has a royalty-free license to exercise all rights under the copyright claimed herein for Governmental Purposes. All other rights are reserved by the copyright owner).

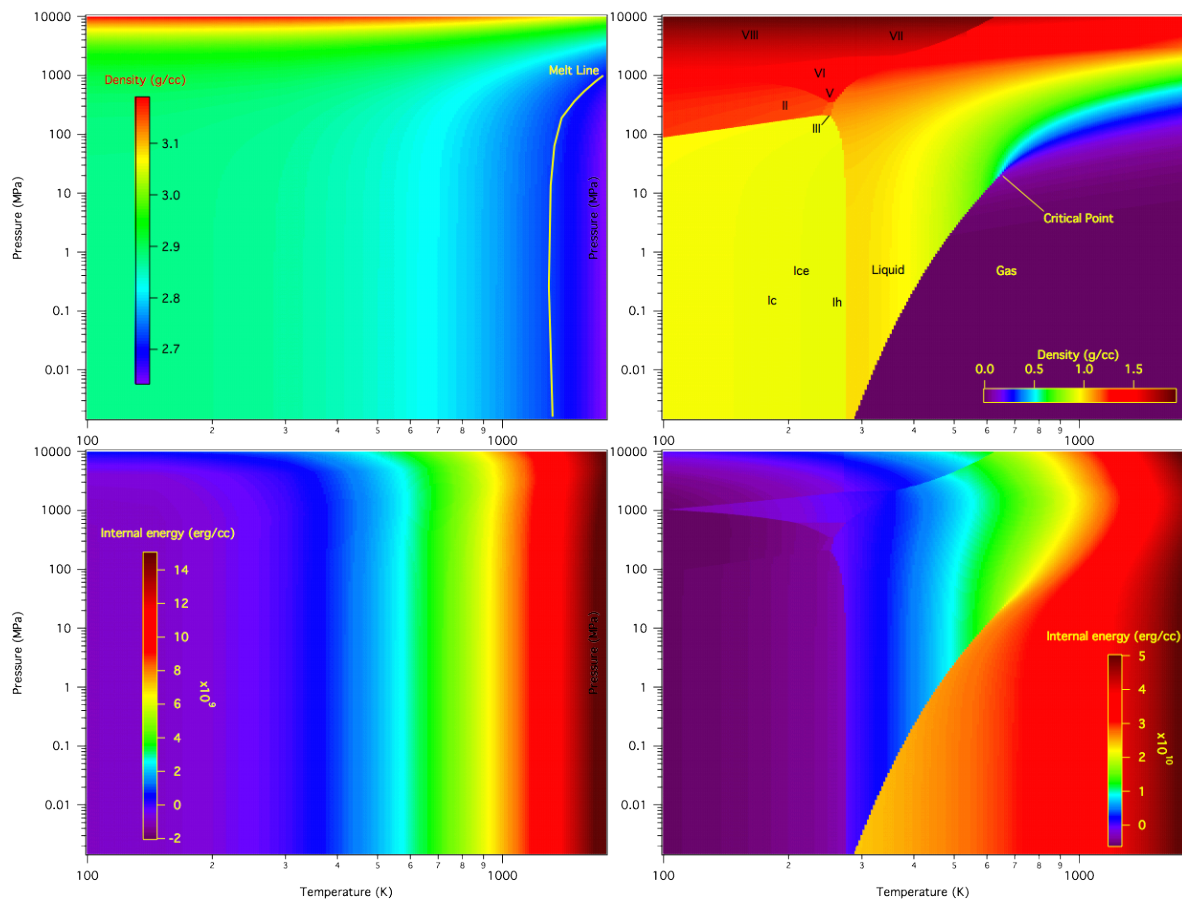


Figure 1. Equations of state for basalt (left) and water (right) as used in the simulations presented here. Basalt (at left) is Sesame material #7530, and water is calculated internally in Sage, from the NBS/NRC Steam tables. The top two charts show density as a function of temperature and pressure, with the dry melt line indicated for basalt and phases indicated for water. The bottom two charts show specific internal energy as a function of temperature and pressure. The very high latent heat of vaporisation for water is easily read from the bottom right frame, as is the high energy density in the supercritical regime.

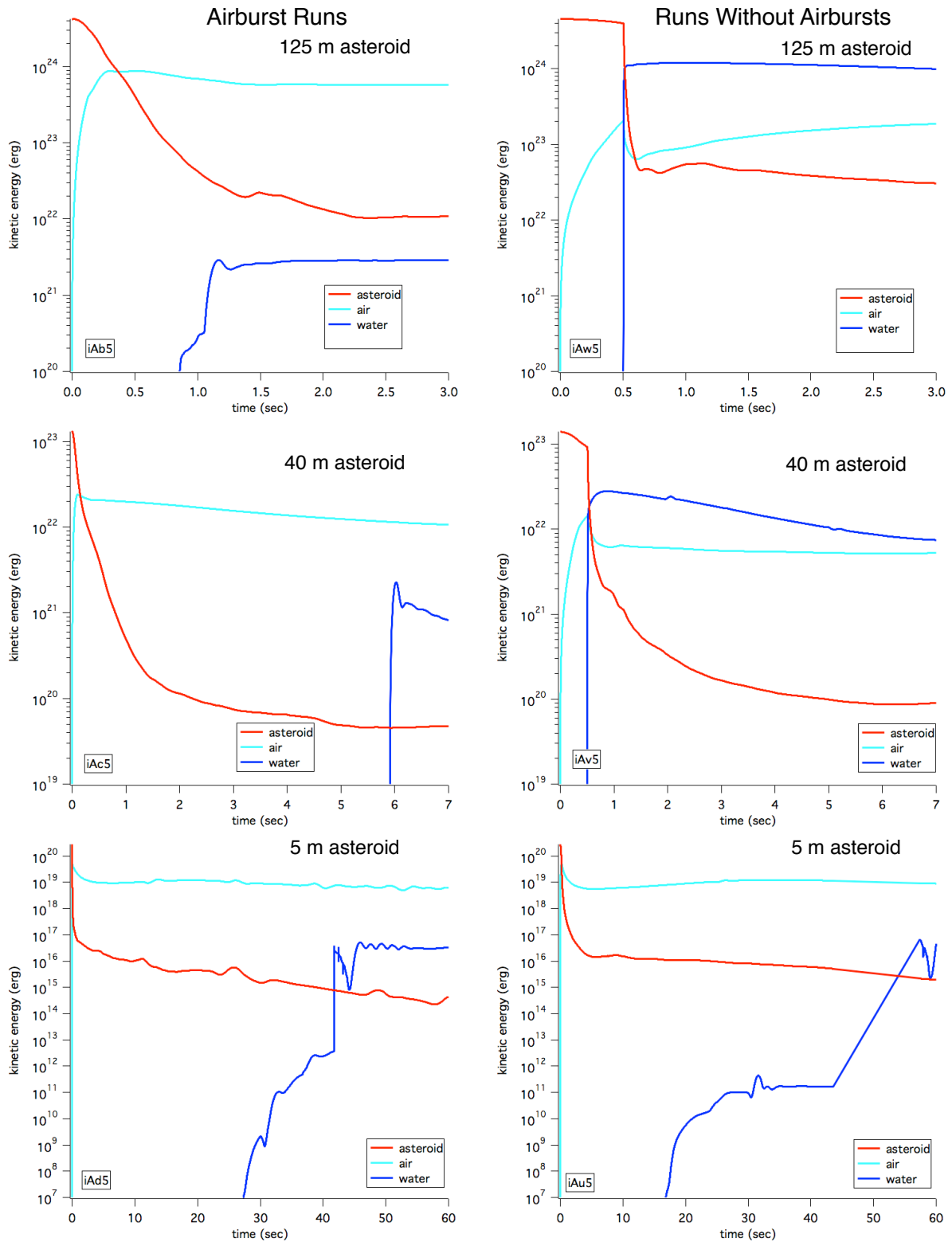


Figure 2. Histories of kinetic energies in the six paired runs of our study. Airburst runs are on the left, non-airburst runs on the right. The top row are the 125-m impact runs, middle row 40-m impacts, bottom row 5-m impacts. A glitch in the energy recording procedure for the 5-m non-airburst case caused the water energy history between 43 and 55 seconds to be lost.

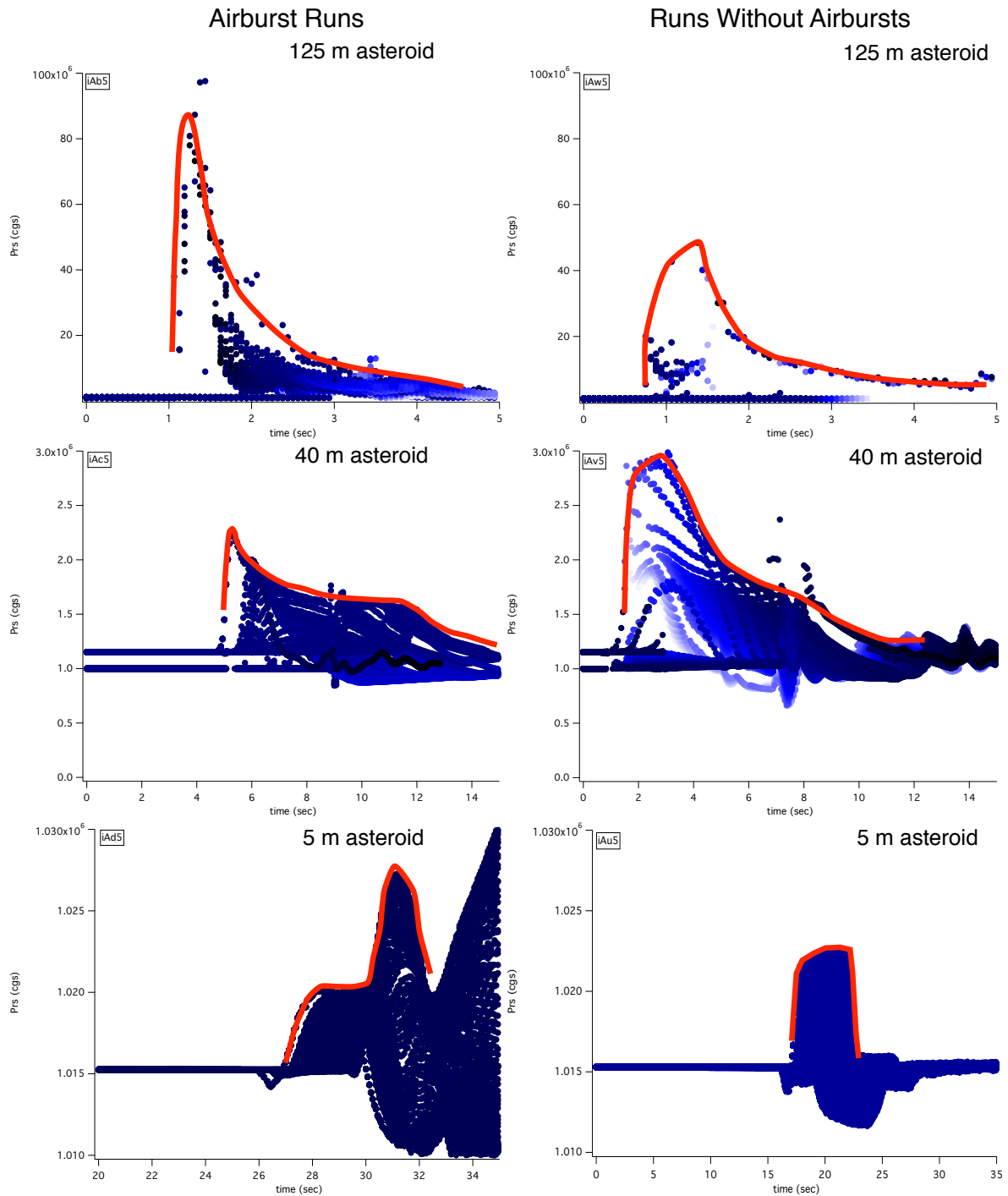


Figure 3. Ground-level pressure histories calculated from tracer particles for each of the six runs. The blue dots are instantaneous pressures recorded by each tracer particle at the time given by the abscissa. The dots are shaded lighter blue for higher particle position, since the particles move during the calculation, although they all start at surface level or 50 m below. The red lines in each plot are drawn by hand to indicate the approximate envelope of pressures experienced at the ground-level.

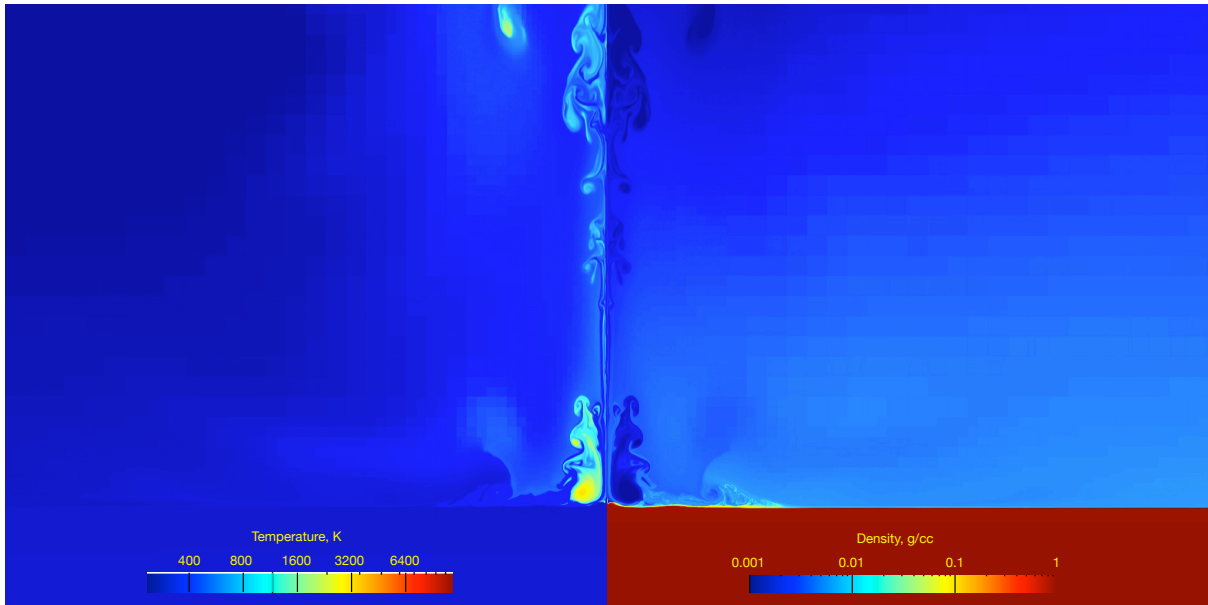


Figure 4. Plot of temperature (left) and density (right) in the calculation (iAb5) of a 125-m asteroid 49 seconds after it experiences an airburst at 10 km altitude, of ~10 MT magnitude. The figure measures 12 km radius vs 12 km height, while the computational domain measures 32 km radius vs 44 km height.

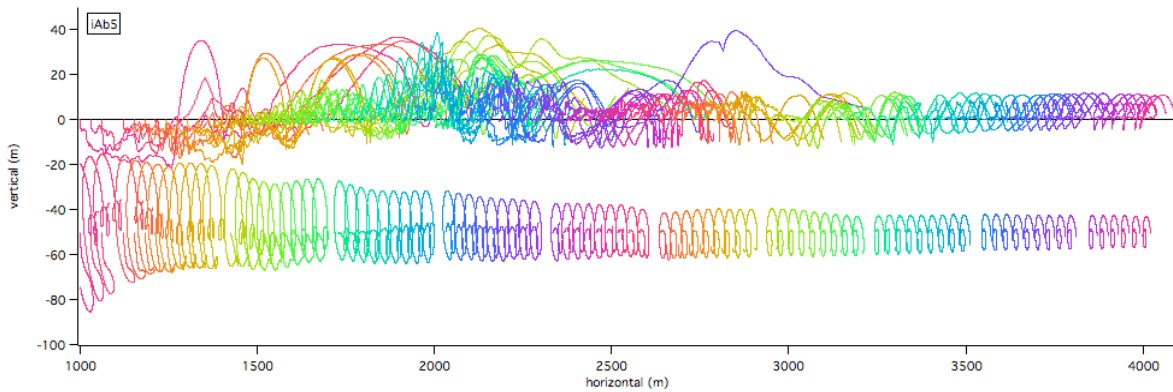


Figure 5. Tracer particle configuration-space trajectories in the calculation (iAb5) of the 125-m asteroid with an airburst. The tracer particles were placed initially in two layers, one at the water surface, the second 50 m below. Note the contrast between the coherent motion of the lower-layer particles with the turbulent motion of those on the surface.

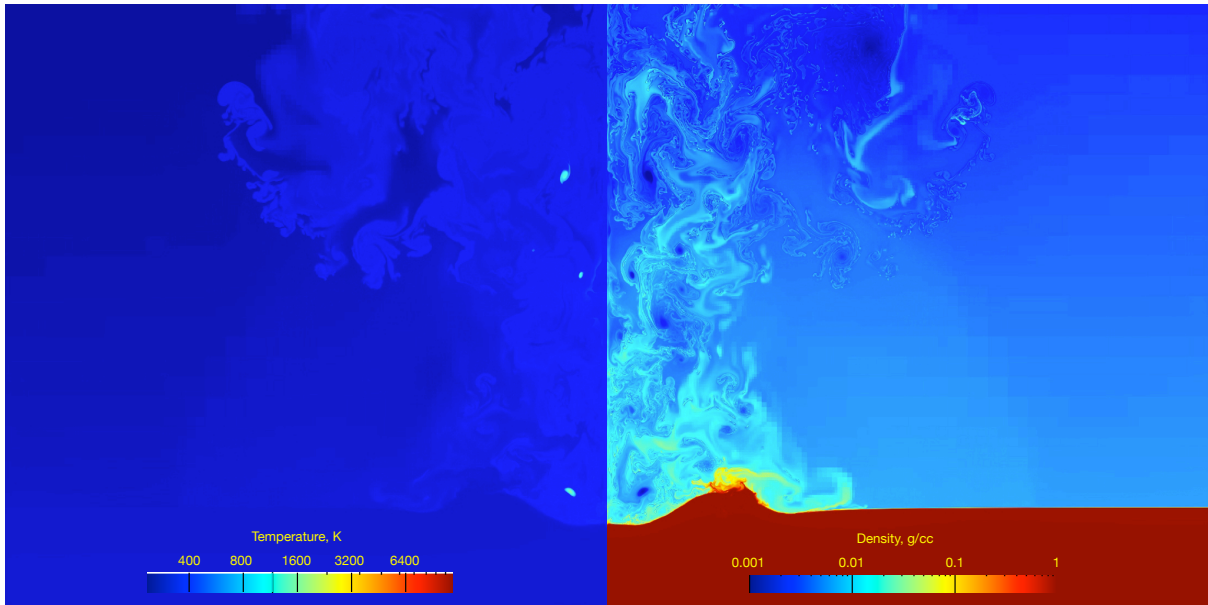


Figure 6. Plot of temperature (left) and density (right) in the calculation of a 125-m asteroid which suffers no atmospheric explosion (iAw5), 63 seconds after impact with the water. The figure measures 12 km radius vs 12 km height, while the computational domain measures 32 km radius vs 44 km height.

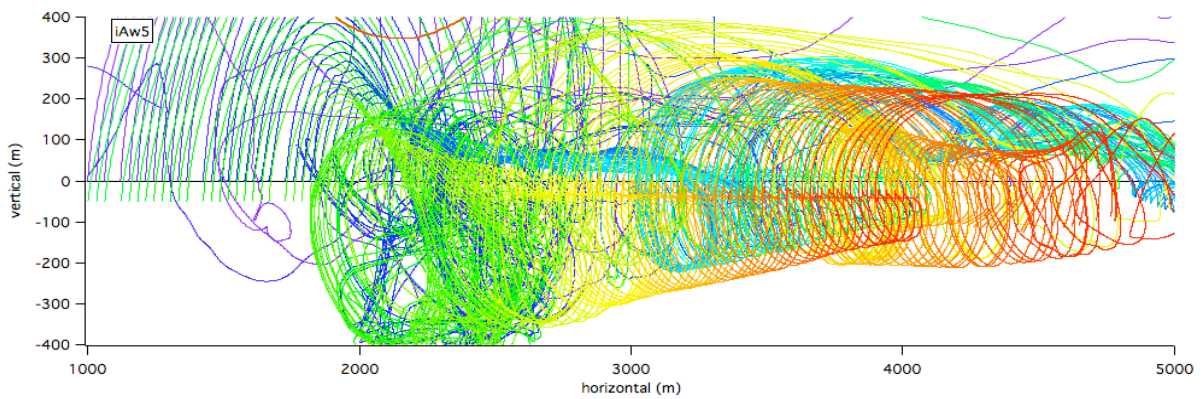


Figure 7. Tracer particle configuration-space trajectories in the calculation (iAw5) of the 125-m asteroid without an airburst. The tracer particles were placed initially in two layers, one at the water surface, the second 50 m below. The direct impact with the water strongly disturbs both the surface and lower-level particles.

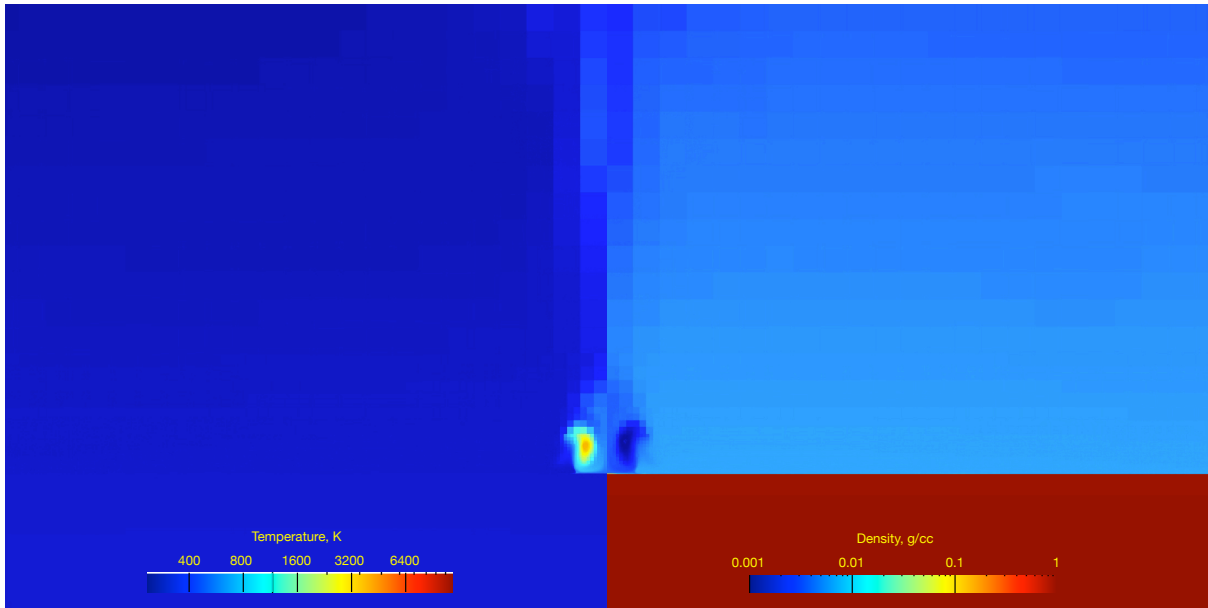


Figure 8. Plot of temperature (left) and density (right) in the calculation (iAc5) of a 40-m asteroid 37 seconds after it experiences an airburst at 10 km altitude, of ~320 kT magnitude. The figure measures 9 km radius vs 9 km height, while the computational domain measures 32 km radius vs 32 km height.

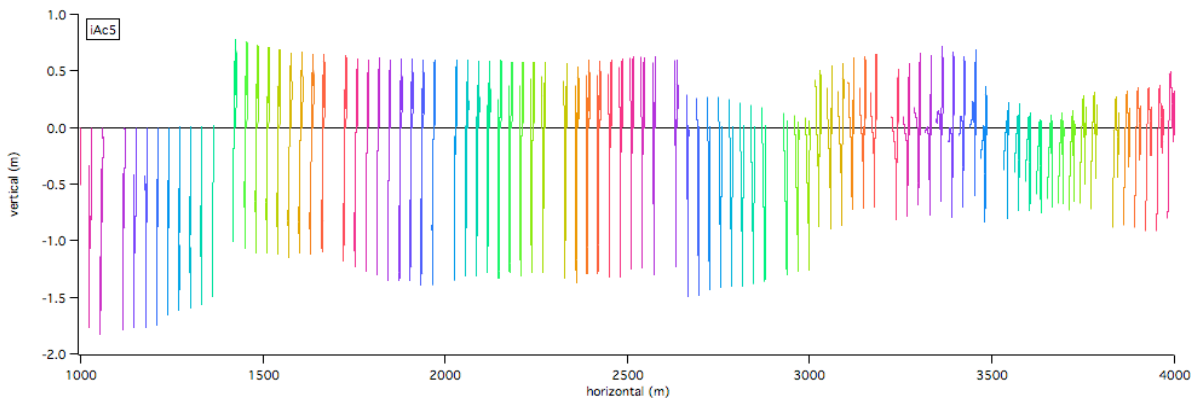


Figure 9. Tracer particle configuration-space trajectories in the calculation (iAc5) of the 40-m asteroid with an airburst. Only the water-surface tracer particles are shown.

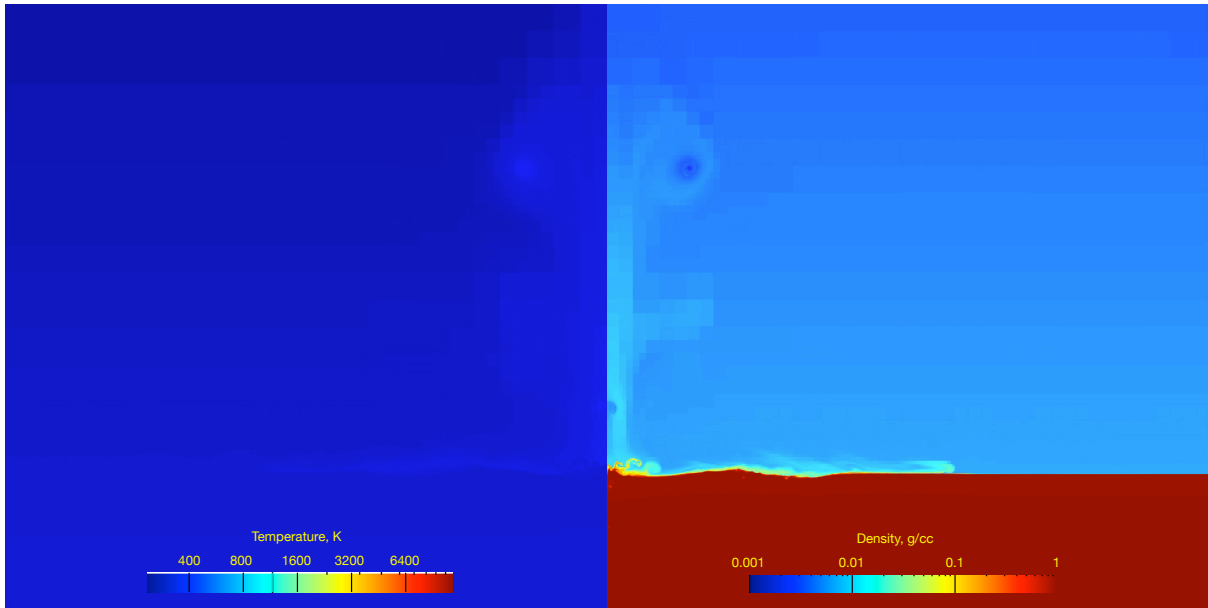


Figure 10. Plot of temperature (left) and density (right) in the calculation (iAv5) of the impact of a 40-m asteroid with no airburst, at 92 seconds after calculation start. The figure measures 9 km radius vs 9 km height, while the computational domain measures 32 km radius vs 32 km height.

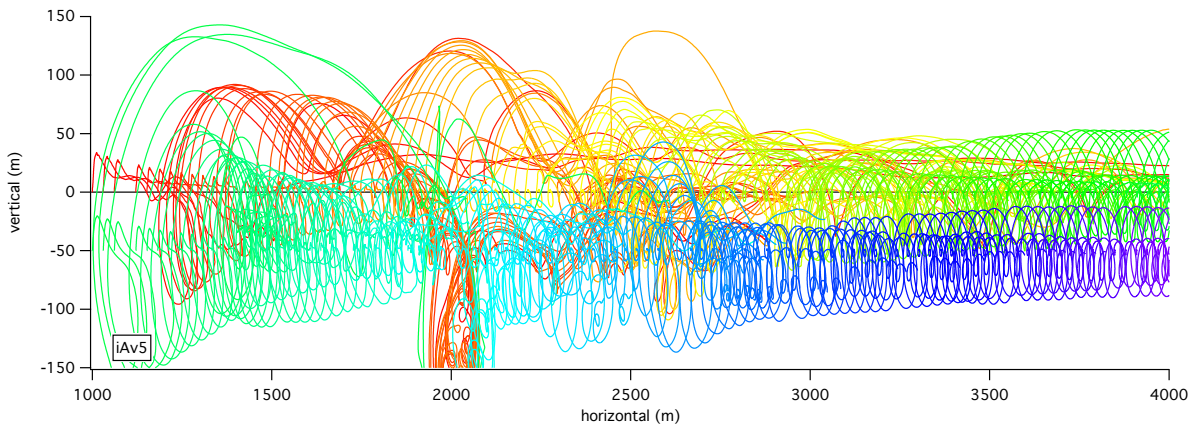


Figure 11. Tracer particle configuration-space trajectories in the calculation (iAv5) of a 40-m asteroid without an airburst. The tracer particles were placed initially in two layers, one at the water surface, the second 50 m below. The direct impact with the water strongly disturbs both the surface and lower-level particles.

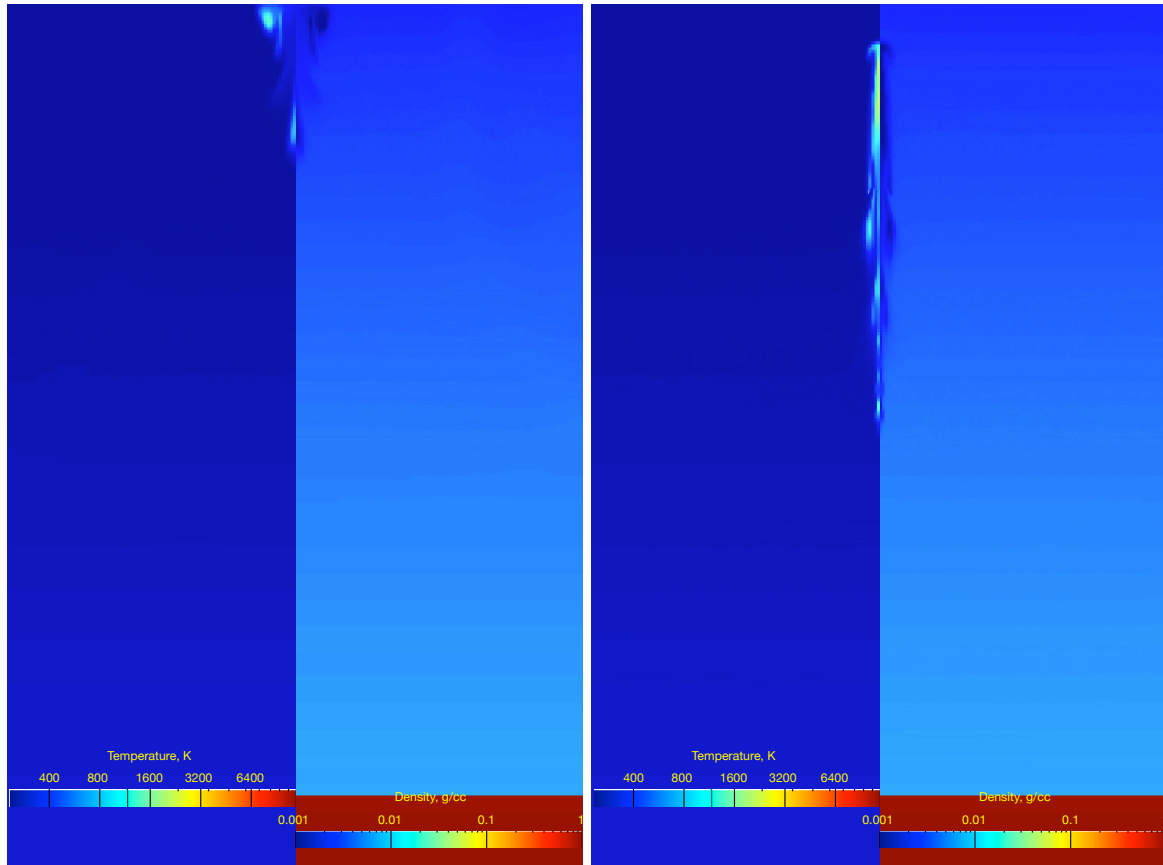


Figure 12. Side-by-side comparison of the 5-m asteroid runs. Left is the run with the airburst at 10 km (iAd5), and right is the run with no airburst (iAu5). In each frame temperature is at left and density at right. Both plots are at 17 seconds after calculation start. Each plot is 4 km in radius and 12 km in height, and depicts the full computational domain.

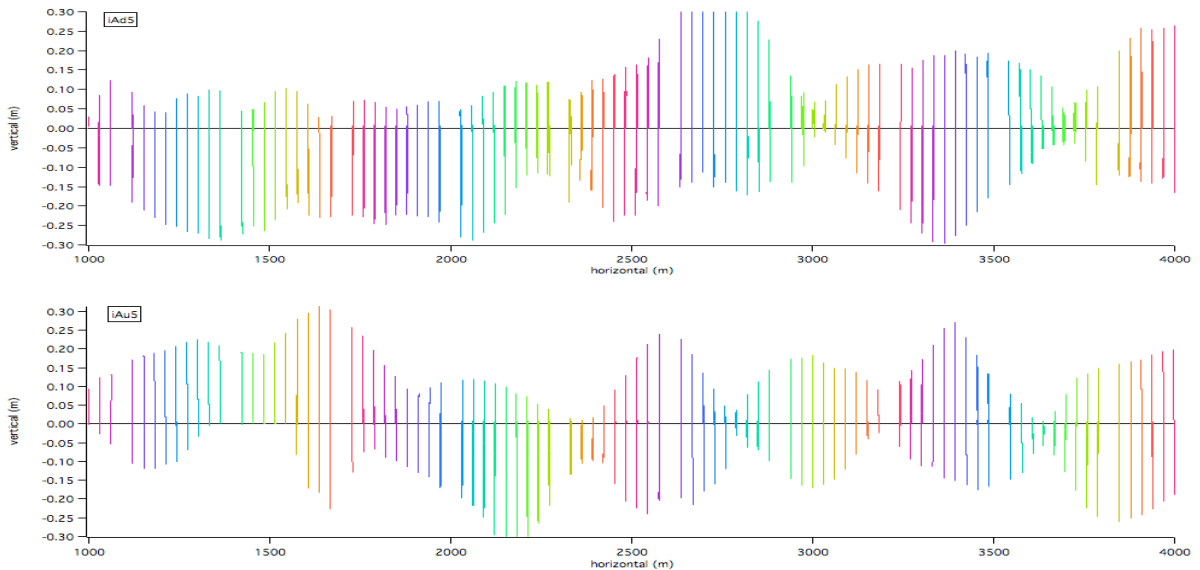


Figure 13. Tracer particle trajectories of the two 5-m asteroid runs. Top is iAd5, with the airburst, and bottom is iAu5, with no airburst. Only the surface row of tracer particles is shown.